

A multiscale consolidation model for press molding of hybrid textiles into complex geometries

Werlen, Vincent; Rytka, Christian; Dransfeld, Clemens; Brauner, Christian; Michaud, Véronique

DOI

[10.1002/pc.28139](https://doi.org/10.1002/pc.28139)

Publication date

2024

Document Version

Final published version

Published in

Polymer Composites

Citation (APA)

Werlen, V., Rytka, C., Dransfeld, C., Brauner, C., & Michaud, V. (2024). A multiscale consolidation model for press molding of hybrid textiles into complex geometries. *Polymer Composites*, 45(6), 5460-5478. <https://doi.org/10.1002/pc.28139>

Important note

To cite this publication, please use the final published version (if applicable). Please check the document version above.

Copyright

Other than for strictly personal use, it is not permitted to download, forward or distribute the text or part of it, without the consent of the author(s) and/or copyright holder(s), unless the work is under an open content license such as Creative Commons.

Takedown policy

Please contact us and provide details if you believe this document breaches copyrights. We will remove access to the work immediately and investigate your claim.

A multiscale consolidation model for press molding of hybrid textiles into complex geometries

Vincent Werlen^{1,2}  | Christian Rytka¹ | Clemens Dransfeld³ |
Christian Brauner¹ | Véronique Michaud² 

¹Institute of Polymer Engineering (IKT), University of Applied Sciences and Arts Northwestern Switzerland (FHNW), Switzerland

²Laboratory for Processing of Advanced Composites (LPAC), Institute of Materials (IMX), Ecole Polytechnique Fédérale de Lausanne (EPFL), Lausanne, Switzerland

³Aerospace Manufacturing Technologies (AMT), Delft University of Technology (TU Delft), Delft, Netherlands

Correspondence

Vincent Werlen, Institute of Polymer Engineering (IKT), University of Applied Sciences and Arts Northwestern Switzerland (FHNW), CH-5210 Windisch, Switzerland.

Email: vincent.werlen@epfl.ch

Funding information

Schweizerischer Nationalfonds zur Förderung der Wissenschaftlichen Forschung; Deutsche Forschungsgemeinschaft

Abstract

Modeling the consolidation of fiber-reinforced thermoplastic composites at the part level presents a formidable computational challenge due to the multi-scale nature of the process. In this article, a method to bypass the multi-scale problem by homogenizing the micro scale and describing the medium with characteristic parameters is described. The model is intended for press molding of hybrid textiles and considers a free-form plate with non-uniform thickness and can describe consolidation in three dimensions with some restrictions. 2D implementation in FEM shows how in-plane matrix pressure gradients can arise in parts and cause fiber disorientation. Experimental verification demonstrates that fiber disorientation arises at the predicted location, and that defect size is proportional to matrix pressure gradient. This novel consolidation model provides new insights, enables part and process optimization, and paves the way for high-quality composite part production.

Highlights

- A consolidation model for press molding of hybrid textiles is presented.
- A method to extend consolidation models for complex geometry is presented.
- The origin of defect formation in complex geometries is explained.

KEYWORDS

consolidation, defects, fiber-reinforced thermoplastic, finite element analysis (FEA), press molding

1 | INTRODUCTION

Hybrid textiles are intermediate materials used in the production of fiber-reinforced thermoplastics. In these materials, continuous reinforcing fibers and polymer are mingled mesoscopically at the textile level. In the case of side-by-side hybrid textiles, the reinforcing fiber plies and thermoplastic plies are alternatively stacked

as shown in Figure 1. Hybrid textiles can be consolidated with processes such as press molding or rapid isothermal stamp forming. Recently, Reynolds et al.¹ reported that stamp forming of hybrid textiles could produce structural parts within a cycle time of only 330 s. If flexible thermoplastic plies such as veils are used, the drapeability of the textile enables the production of semi-complex parts.

This is an open access article under the terms of the [Creative Commons Attribution-NonCommercial-NoDerivs](https://creativecommons.org/licenses/by-nc-nd/4.0/) License, which permits use and distribution in any medium, provided the original work is properly cited, the use is non-commercial and no modifications or adaptations are made.

© 2024 The Authors. *Polymer Composites* published by Wiley Periodicals LLC on behalf of Society of Plastics Engineers.

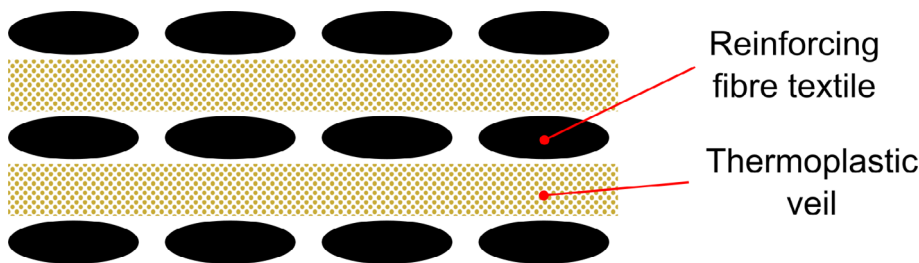
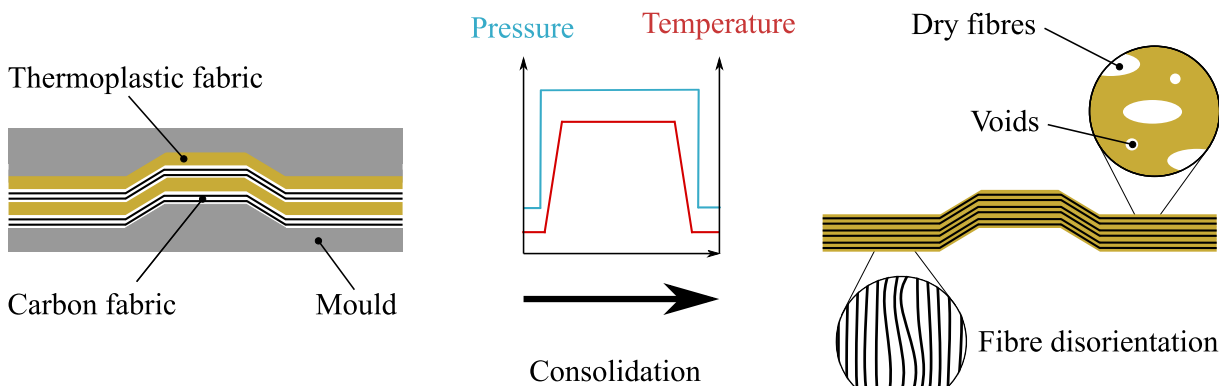


FIGURE 1 Schematic representation of a hybrid side-by-side textile with a veil as thermoplastic ply.

(A)



(B)

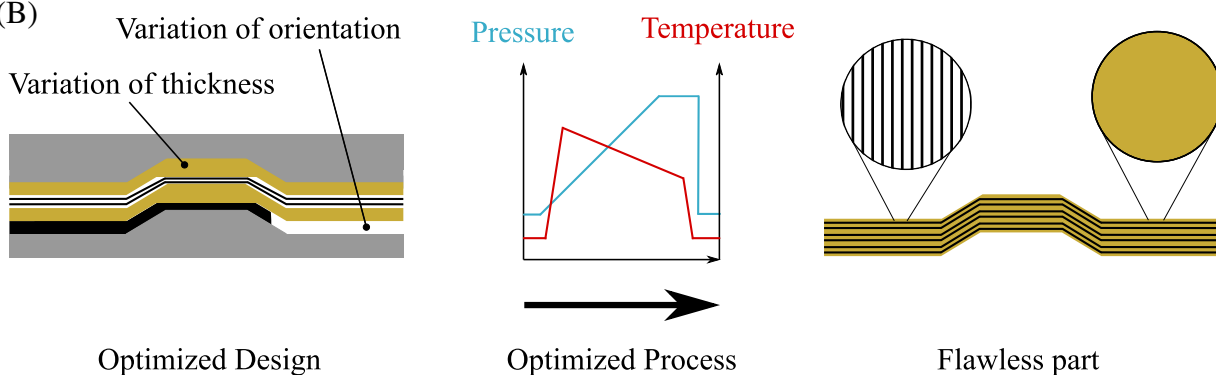


FIGURE 2 (A) Representation of state-of-the art consolidation of hybrid textiles. For complex shapes defects such as depicted on the right might occur. The consolidation model presented in this study enables the prediction of such defects. (B) Representation of an optimized consolidation process where appropriate selection of the design and process parameters prevents defect formation.

One of the key advantages of hybrid textiles is their high design flexibility. Many parameters can be easily or locally changed, including the orientation or textile architecture of each layer, the thickness of the thermoplastic ply to influence the fiber volume fraction, and the addition of material in local areas. This allows the composite properties to be tailored for specific applications, making it possible to combine high performance with geometrical complexity. In addition, using appropriate processes such as rapid isothermal press molding could also keep the cycle times competitive.

Despite these compelling advantages, the current lack of a three-dimensional consolidation model has been a

major obstacle to their successful development and implementation. Defects, such as porosities caused by incomplete impregnation or fiber disorientation resulting from in-plane matrix flow, cannot yet be predicted. A three-dimensional consolidation model would not only allow to predict of the occurrence of such defects but also enable design or process optimization in order to produce high-quality, defect-free parts as shown in Figure 2.

The consolidation of fiber-reinforced composites involves several physical phenomena occurring at the micro, meso, and macro levels, such as matrix flow, ply compaction, and bubble formation or collapse.²⁻⁴ All of these phenomena have been extensively studied and are

currently well understood.^{5–11} Several models have been proposed for each phenomenon, usually these are valid for specific materials and processes as these heavily influence the underlying effects. This implies that the validity range of a consolidation model will be subjected to the same limitations of the models describing the underlying effects upon which it is built.

Regarding fiber movement, for instance, Schuler and Advani¹² found that the fiber-matrix continuum in unidirectional plies behaves as a fluid transversally to the fibers. If the flow field is not homogeneous, fiber-matrix flow can cause fiber disorientation and waviness, which can significantly alter the mechanical properties.¹³ Several authors subsequently proposed models for fiber-matrix flow based on the work of Schuler and Advani.^{14–17} However, the fiber-matrix continuum does not behave as a fluid in the fiber direction because the fibers restrict flow in that direction. Therefore, for woven textiles where fibers are oriented in different directions along which they restrict flow, the fiber-continuum cannot be described as a fluid in any direction.¹² Recent investigations by Hautefeuille et al.^{18,19} suggest that for woven textiles there is a threshold in matrix pressure gradient below which percolation regime takes place and above which fiber-matrix flow causing fiber disorientation occurs. Yet, models able to predict fiber disorientation and its extent are still lacking.

Void formation is another material-dependent phenomenon: in thermosets composites volatiles are emitted as a result of curing, which leads to the formation of bubbles. Porosities can also result from incomplete impregnation or from matrix shrinkage upon curing. Different models were proposed to describe bubble formation and collapse in thermosets, and are well established.^{10,11,20} In thermoplastic composites voids can be created by entrapped air or by crystallization shrinkage.^{21–24}

Developing a three-dimensional consolidation model is challenging, as the different effects influence each other and the volume is not conserved as voids get filled during impregnation. Therefore, simply adding the models for the different phenomena taking place during consolidation is not possible. Developing a full-scale simulation is also difficult due to the multi-scale nature of the process, which represents a formidable computational challenge. Moreover, the complex interactions between textile, matrix, and air at both the micro and macro levels make their description difficult. While several authors presented three-phase models either for composite processing^{25,26} or earth science,^{27,28} these are single-scale flow models that cannot consider the impregnation of fiber bundles nor its influence on the matrix pressure. Models that consider dual scale flow^{29,30} on the other hand typically do not consider textile compaction or the change of volume due to impregnation of fiber bundles. Few authors proposed three-dimensional

consolidation models that took into account all of these effects. Wysocki et al. attempted to model consolidation with a two-phase continuum framework and entropy inequality,^{2,3,31} a similar approach was followed by Rouhi et al.^{32–34} In both cases, the difficulty to determine the values of variables related to the entropy inequality equation make their implementation challenging in practice.

When it comes to models at the level of a unit cell, however, a large body of work is available in the literature. These analytical models can be described as zero-dimensional, in the sense that variations of properties or parameters such as pressure or impregnation degree in any direction cannot be considered. Therefore, potential phenomena arising during consolidation and especially for complex shapes, such as in-plane and through-thickness material flow, are typically missing. Moreover, the change of volume due to impregnation and the resulting textile deformation and compaction is usually disregarded in available consolidation models. Most of the consolidation models at the level of a unit cell presented so far focus on modeling matrix flow in fiber bundles to predict impregnation degree and porosity.^{35–40} Jespersen et al.⁴¹ a proposed one-dimensional consolidation model in the through-thickness direction that can account for matrix flow based on the work of Michaud et al.^{6,7,42,43} and Sommer and Mortensen,⁴⁴ which model the impregnation of a compressible fiber mat.

Most of the authors assumed that air could freely escape the tow. Others, such as Bernet et al.⁵ in their model about the consolidation of commingled yarns, introduced a threshold during impregnation after which the air gets entrapped. Rozant et al.³⁶ considered that air was trapped in the tows during the whole process in their model about the consolidation of knits, but did not consider dissolution. Several studies highlighted the difficulty in obtaining full consolidation in fibrous reinforcement due to internal voids.^{23,45} The experimental validation of consolidation models presented by many authors shows poor accuracy in predicting the voids of fully consolidated composites. Yet, correct prediction of the final void content is relevant in composite production as it is detrimental to mechanical properties.^{22,46}

Recently, Werlen et al.⁴⁷ proposed and validated a model for the consolidation of hybrid textiles in which air entrapment and dissolution within the tow is considered, and demonstrated that it significantly influences consolidation. The approach proved to be able to accurately predict porosity content, even in fully consolidated composites with low void content. Yet, the model complexity remains zero-dimensional and a three-dimensional extension is desirable in order to simulate the consolidation of complex-shaped parts.

In this article, the consolidation model recently proposed by Werlen et al.⁴⁷ is extended and implemented

three-dimensionally in a way suitable for finite-element implementation and experimentally verified. The model considers a free-form plate with changing thickness and constant through-thickness properties and neglects any textile deformation. Since draping usually takes place before consolidation, the consolidation model presented here could be used in combination with existing models such as the one presented in.^{48–50}

The consolidation model can predict parameters such as fiber volume and porosity content locally in a three-dimensional manner and takes into account in-plane matrix flow, as opposed to most of the current models for the consolidation of hybrid textiles. Additionally, the novel homogenization approach allows to consider a change of volume as a result of in-plane matrix flow and impregnation. Compared to existing three-dimensional models, the model has the advantage that parameters can be easily identified through material characterization. The proposed consolidation model can identify areas with elevated matrix pressure gradients that are prone to defect formation. The study demonstrates that matrix pressure and impregnation degree in three-dimensional parts are non-uniform and that pressure gradients can cause fiber disorientation, leading to defects whose magnitude is proportional to the maximum matrix pressure gradient during consolidation.

2 | APPROACH

In order to derive the constitutive equations for the three-dimensional consolidation of thermoplastic composites, a homogenization method based on a unit cell approach and a consolidation model were adopted. While the consolidation model proposed by Werlen et al.⁴⁷ was selected for this study, the methodology presented here is intended to be more general and applicable to other models as well. This homogenization method avoids the need for numerically expensive full-scale simulations at both the macro and

micro levels. Instead, finite element analysis is performed only on the homogenized medium at the macro level. Despite this simplification, the state of the homogenized medium remains well described by a set of descriptors, such as the impregnation degree or the fiber volume fraction.

During consolidation, the medium at hand is a three-phase mixture constituted of the liquid matrix, the solid fibers, and air. At the beginning of consolidation, the tows are dry and surrounded by completely molten polymer which fills the inter-tow space. In the tows, an initial quantity n_0 of air is entrapped. The initial conditions and assumptions regarding consolidation are the same as in the consolidation model of Werlen et al.,⁴⁷ where these are stated in greater detail.

A free-form plate with non-uniform thickness, as shown in Figure 3, is considered. It is assumed that all the properties of the plate at the micro and mesoscopic scale, such as fiber volume fraction, tow shape, or impregnation degree are constant through thickness at a given time.

It is assumed that the tows are incompressible and that there is no fiber disorientation during consolidation while shearing of the textile plies is neglected. While the model is strictly speaking not valid for consolidation with fiber disorientation, the effect is local so it is safe to assume that the effects on the consolidation at the part level can be neglected. In addition, the three-phase mixture is assumed to be deformable only in the normal direction to the textile plane orientation. In a standard press molding process the mold is closed only in one direction, perpendicular to the overall in-plane direction which is neither extended nor compressed.

A unit cell is considered here, which will be used to derive the equations for the homogenized medium. The unit cell is obtained by discretizing the free-form plate in both in-plane directions to obtain trapezoids containing the three-phase mixture with a number of portions of tow as shown in Figure 3. The trapezoid has a width Δx , a depth Δy , and a height h spanning the whole local

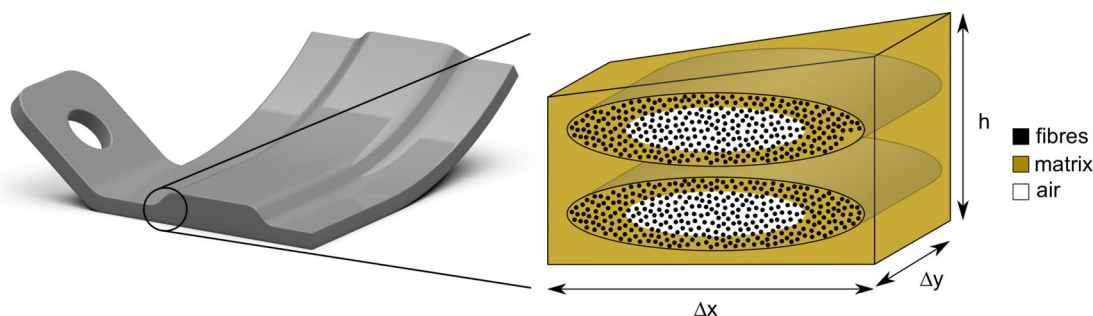


FIGURE 3 Example of a free-form plate with non-uniform thickness and constant through-thickness properties, which corresponds to the geometrical complexity addressed by the model in this study. The part is discretized into unit cells that have a trapezoidal shape as represented on the right, which contains a three-phase mixture consisting of air, fibers, and matrix. The inter-tow space is completely filled with molten polymer, while the intra-tow space is occupied by matrix and air.

thickness of the plate since the plate is not discretized through-thickness. Since the unit cell is a trapezoid, h depends linearly on x and y in order to be able to capture variations in thickness. The unit cell is constructed around the reinforcing textile, and the z direction of either the unit or homogenized medium is always normal to the local plane formed by the textile. The unit cell has fixed width Δx and depth Δy while the four edge heights can vary according to the aforementioned assumptions. In-plane matrix flow is allowed across the boundaries to reflect in-plane matrix flow resulting from pressure gradient. However, no fiber crosses the boundaries as the unit cell is centred around it.

3 | CONSTITUTIVE EQUATIONS

3.1 | Medium descriptors

The consolidation model is written based on volume fractions formulation since a continuum formulation is sought. The fiber volume fraction ν_f is defined as the ratio of the volume of a given entity over the total volume. While the matrix, gas and meso fiber volume fractions ν_m , ν_g , and ν_f are defined over the unit cell volume, the tow fiber volume fraction $\nu_{f,tow}$ is defined over the tow volume as expressed through Equation (1). Thereby, the unit cell volume V , density ρ and mass M are related through Equation (2):

$$\nu_m = \frac{V_m}{V} \quad \nu_g = \frac{V_g}{V} \quad \nu_f = \frac{V_f}{V} \quad \nu_{f,tow} = \frac{V_f}{V_{tow}} \quad (1)$$

$$M_m = \rho_m V_m \quad M_f = \rho_f V_f \quad (2)$$

where the subscripts f , m and g indicate that the property is related to respectively fiber, matrix, or gas, and V_{tow} is the space occupied by the tows, which includes the interstitial space between the fibers. The different volumes such as V_{tow} and V_g , refer to the sum of the volume of all the portions of tows inside the unit cell and not a single particular tow. The sum of the volumes of the different phases add up to the total volume and it therefore holds, by inserting Equation (1):

$$V_m + V_f + V_g = V \quad \nu_m + \nu_f + \nu_g = 1 \quad (3)$$

The tow impregnation degree is defined as the volume of impregnated tow $V_{tow,impr}$ divided by the volume occupied by the tow V_{tow} :

$$\xi = \frac{V_{tow,impr}}{V_{tow}} \quad (4)$$

It is assumed that void consists solely of the space between the fibers of the unimpregnated tow, where air is entrapped. Therefore, porosity and gas volume fraction are equivalent and one can establish a relation for V_g and describe ν_g by inserting Equations (4) and (1) as following:

$$V_g = (V_{tow} - V_{tow,impr})(1 - \nu_{f,tow})$$

$$\nu_g = \nu_f(1 - \xi) \frac{(1 - \nu_{f,tow})}{\nu_{f,tow}} \quad (5)$$

3.2 | Constitutive equations

Mass conservation is applied to the unit cell, shown in Figure 3, to derive equations for the continuum. Considering that the fibers remain in the unit cell and have constant density, one can write, using Equation (2):

$$\frac{\partial M_f}{\partial t} = 0 \quad \frac{\partial \rho_f}{\partial t} = 0 \quad \frac{\partial V_f}{\partial t} = 0 \quad (6)$$

For the mass conservation of matrix the flux needs to be taken into account, with constant matrix density ρ_m and with Equation (2) it holds:

$$\frac{\partial M_m}{\partial t} = \frac{\partial V_m \rho_m}{\partial t} = \rho_m \frac{\partial V_m}{\partial t} \quad (7)$$

Equations (1), (3), (5), and (6) can be combined to yield, as detailed in Appendix A:

$$\frac{\partial \nu_f}{\partial t} = -\frac{\nu_f}{V} \frac{\partial V_m}{\partial t} + \nu_f^2 \frac{1 - \nu_{f,tow}}{\nu_{f,tow}} \frac{\partial \xi}{\partial t} \quad (8)$$

$$\frac{\partial \nu_g}{\partial t} = (\nu_g - 1) \left(\nu_f \frac{1 - \nu_{f,tow}}{\nu_{f,tow}} \frac{\partial \xi}{\partial t} \right) - \frac{\nu_g}{V} \frac{\partial V_m}{\partial t} \quad (9)$$

To resolve the temporal change of matrix volume, which is directly linked to the in-plane matrix flow, Darcy's law⁵¹ is applied and the unit cell and discretized as detailed in Appendix B. Inserting the result back in the equations yields:

$$\frac{\partial \nu_f}{\partial t} = \nu_f^2 \frac{1 - \nu_{f,tow}}{\nu_{f,tow}} \frac{\partial \xi}{\partial t} - \frac{\nu_f}{\eta} \left(\vec{\nabla} K \vec{\nabla} P_m + \frac{\vec{\nabla} h^T K \vec{\nabla} P_m}{h} \right) \quad (10)$$

$$\frac{\partial \nu_g}{\partial t} = (\nu_g - 1) \left(\nu_f \frac{1 - \nu_{f,tow}}{\nu_{f,tow}} \frac{\partial \xi}{\partial t} \right) - \frac{\nu_g}{\eta} \left(\vec{\nabla} K \vec{\nabla} P_m + \frac{\vec{\nabla} h^T K \vec{\nabla} P_m}{h} \right) \quad (11)$$

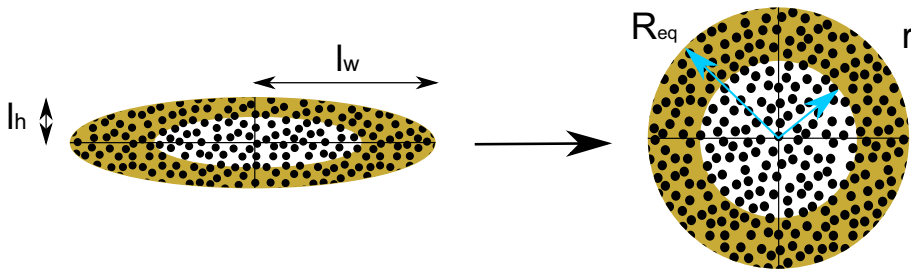


FIGURE 4 Schematic representation of the equivalent geometry. Reproduced with permission from.⁴⁷

whereas K is a second order diagonal tensor with permeability K_x and K_y in x and y direction, which depends on the fiber volume fraction.^{4,52,53}

$$K = \begin{pmatrix} K_x & 0 \\ 0 & K_y \end{pmatrix} \quad (12)$$

$$\xi = \frac{R_{eq}^2 - r^2}{R_{eq}^2} \quad (13)$$

3.3 | Consolidation model

In the following, the consolidation model proposed by Werlen et al.⁴⁷ is implemented to resolve the temporal change of impregnation degree $\frac{\partial \xi}{\partial t}$. This model describes the impregnation of an elliptical tow with semi major and minor axis l_w and l_h by considering an equivalent round tow with radius R_{eq} , radius to the flow front r as shown in Figure 4, and similar impregnation kinetics. Because of the assumptions of homogeneous variables in the through-thickness direction, all the tows inside an unit cell and their impregnation kinetics are identical, therefore considerations about a single tow can be extended to the whole unit cell. For instance, the tow impregnation degree can be related to the equivalent radius following⁴⁷:

In the consolidation model proposed by Werlen et al.⁴⁷ the flow front behavior is described by resolving Equation (14). Expressing $\frac{\partial \xi}{\partial t}$ on the basis of Equation (13) and combining it with Equation (14) allows to obtain Equation (15), as detailed in Appendix C:

$$r \cdot \ln\left(\frac{r}{R_{eq}}\right) \frac{\partial r}{\partial t} = \frac{K_{tow}(P_m + P_c - P_g)}{\eta(1 - \nu_{f,tow})} \quad (14)$$

$$\frac{\partial \xi}{\partial t} = \frac{-2K_{tow}(P_m + P_c - P_g)}{R_{eq}^2 \eta(1 - \nu_{f,tow}) \ln(\sqrt{1 - \xi})} \quad (15)$$

In this equation, K_{tow} is the tow permeability and P_m , P_c , and P_g are respectively the matrix, capillary, and gas pressure. All the assumptions, considerations and equations of the consolidation model, including those to

obtain P_m and P_g are described in detail in.⁴⁷ In that publication, the capillary pressure P_c was considered small in comparison with the elevated matrix pressure and neglected, which is also the approach adopted here. The tow fiber volume fraction is assumed to remain constant here as it was found in other articles to have a weak dependence on applied pressure.^{4,47} Since Equation (15) results in an infinite rate of impregnation at $\xi = 0$, an appropriately chosen small value ϵ has to be selected as initial condition for numerical stability.

The tow permeability K_{tow} is largely influenced by the tow fiber volume fraction, which depends on the applied pressure. Therefore, one can model the tow permeability as a function of the applied pressure despite the assumption of a constant tow fiber volume fraction. By describing K_{tow} as a function of the applied pressure through the function $A_{tow} \cdot \log_{10}(P_{app}) + B_{tow}$ and inserting it into the model of Gebart⁵³ for the permeability of unidirectional reinforcements one obtains Equation (16), where R_f is the fiber radius. More detailed informations are provided in Werlen et al.⁴⁷

$$K_{tow} = \frac{16}{9\pi\sqrt{6}} R_f^2 \cdot \left(\sqrt{\frac{\pi}{2\sqrt{3}(A_{tow} \cdot \log(P_{app}) + B_{tow})} - 1} \right)^{\frac{5}{2}} \quad (16)$$

The gas pressure of the entrapped gas is obtained on the basis of the ideal gas law in Equation (17), thereby the initial amount of entrapped gas n_λ^0 is given by Equation (18) and the variation of the amount of entrapped gas \dot{n}_λ is described through Equation (19).

$$P_g = \frac{n_\lambda \cdot R \cdot T}{A_{tow} \cdot (1 - \nu_{f,tow}) \cdot (1 - \xi)} \quad (17)$$

$$n_\lambda^0 = \frac{P_{atm} \cdot A_{tow} \cdot (1 - \nu_{f,0} \cdot \nu_{f,tow})}{R \cdot T_0 \cdot \nu_{f,0}} \quad (18)$$

$$\dot{n}_\lambda = -2 \cdot \pi \cdot r \cdot G \cdot D \cdot (C_s - C_\infty) \cdot \left(1 + \frac{1}{\sqrt{\pi D G t}} \right) \quad (19)$$

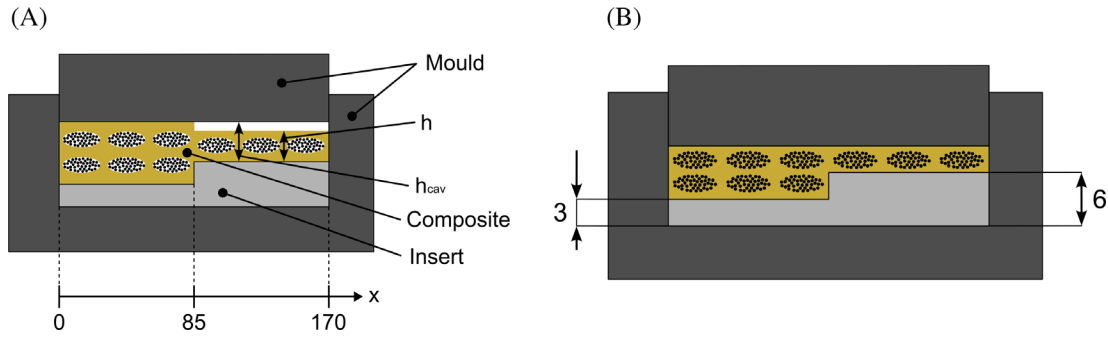


FIGURE 5 Schematic representation of the mold containing an insert to produce a plate with changing thickness with dimensions in mm (A, B) represents, respectively, the unconsolidated and fully impregnated state. (A) The meso structure of the hybrid textile already collapsed and matrix completely fills the inter-tow space, as per the assumptions of the consolidation model. Because the void volume per unit area is larger in the thicker part of the mold, at the beginning of consolidation only the thick part is in contact with the mold. The tows are here shown schematically and the scale is not respected, as in the case study and in the experiments there are more layers of the glass textile fabric.

where A_{tow} is the cross-sectional area of the tow, R the ideal gas constant, T the temperature, n^0_λ the initial amount of entrapped gas per unit depth in each tow, P_{atm} the atmospheric pressure, $\nu_{f,0}$ the fiber volume fraction of the textile stack at rest, T_0 the temperature at the beginning of consolidation, D the diffusion of air in molten polymer, G the correction factor for diffusion in fibrous medium, C_s the saturation concentration at the air-polymer interface, and C_∞ the saturation concentration at atmospheric pressure. These three equations are taken from Werlen et al.,⁴⁷ where they are described in greater detail.

3.4 | Boundary conditions

For the boundary conditions an infinitely stiff guided mold is considered with an exact control system such that the cavity height or applied pressure perfectly corresponds to the prescribed one. This implies that the change of cavity height h_{cav} is the same everywhere in the mold and the closing speed v_{close} is defined as:

$$v_{close} = \frac{\partial h_{cav}}{\partial t} \quad (20)$$

The closure rate of the mold will translate to the composite and act as a boundary condition, but only if both are in contact. Therefore, the local rate v at which the composite thickness h changes reads:

$$v = \frac{\partial h}{\partial t} = \begin{cases} v_{close} & h = h_{cav} \\ 0 & h < h_{cav} \end{cases} \quad (21)$$

The composite thickness h and cavity height h_{cav} are schematically represented in Figure 5A. The local change of composite thickness is related to in-plane matrix flow

and impregnation, which results in the composite taking up less space as the volume occupied by the gas phase is reduced. In the unit cell, whose width Δx and depth Δy are constant, simple geometrical considerations allow to relate the change of volume and thickness as following:

$$V = \Delta x \cdot \Delta y \cdot h \quad \frac{\partial V}{\partial t} = \Delta x \cdot \Delta y \cdot \frac{\partial h}{\partial t} \quad (22)$$

Combining these equations as described in Appendix D transforms Equation (21) into:

$$\frac{v}{h} = \frac{\vec{\nabla} K \vec{\nabla} P_m}{\eta} + \frac{(\vec{\nabla} h)^T K \vec{\nabla} P_m}{h \cdot \eta} - \nu_f \frac{1 - \nu_{f,tow}}{\nu_{f,tow}} \frac{\partial \xi}{\partial t} \quad (23)$$

Within industrial manufacture mostly an applied force F_{app} is prescribed to the press and acts as boundary condition. Equation (23) always holds true with the aforementioned assumptions, therefore the closing speed which will require the prescribed amount of applied force is sought:

$$v_{close} \left| \int \int (P_m + P_c - P_g) dx dy = \int \int P_{app} dx dy = F_{app} \quad (24)$$

Thereby, the mechanical equilibrium between applied pressure P_{app} , matrix pressure P_m and textile stress response σ_{tex} as described in Werlen et al.⁴⁷ applies:

$$P_m = P_{app} - \sigma_{tex} \quad (25)$$

In this article, no direct formulation to solve Equation (24) is proposed. Instead, iterative optimization

methods are used to find the value of v_{close} satisfying the boundary condition.

Another boundary condition has to be defined at the edge of the composite, where contact with the tool prohibits any in-plane flow. Thus, the boundary condition at the edges reads, assuming a perfectly sealed mold:

$$\frac{\partial P_m}{\partial n} = 0 \quad (26)$$

Thereby, n is a vector perpendicular to the local tool wall.

3.5 | Initial conditions

It is considered that the local amount of fibers and matrix are known, and that at the beginning of consolidation the tows are completely dry. The mold is manufactured to match the geometry of the fully consolidated plate, neglecting any in-plane matrix flow. The local height of the composite can be formulated with Equations (27), as detailed in Appendix E:

$$h = \frac{N \cdot M_m^A}{\rho_m} + \frac{N \cdot M_f^A}{\rho_f} \left(1 + (1 - \xi) \cdot \frac{1 - \nu_{f,tow}}{\nu_{f,tow}} \right) \quad (27)$$

Where M_M^A and M_f^A are the local areal weight in a single layer of respectively the matrix and the fibers, N is the number of hybrid textile layers, and an impregnation degree ξ of 0 and 1 is inserted to obtain respectively the initial and final local plate thickness h_{start} and h_{end} . The initial fiber, matrix and volume fraction ν_f^{start} , ν_m^{start} , and ν_g^{start} at the beginning of impregnation read, as described in Appendix D and assuming an impregnation degree ξ of 0 at the beginning of consolidation:

$$\begin{aligned} \nu_f^{start} &= \frac{N \cdot M_f^A}{\rho_m \cdot h_{start}} \\ \nu_m^{start} &= \frac{N \cdot M_m^A}{\rho_m \cdot h_{start}} \\ \nu_g^{start} &= \frac{N \cdot M_f^A}{\rho_f \cdot h_{start}} \frac{1 - \nu_{f,tow}}{\nu_{f,tow}} \end{aligned} \quad (28)$$

4 | MATERIALS AND MATERIAL CHARACTERIZATION

In this study, a quasi-unidirectional (UD) Leno glass fiber woven fabric with an areal weight of 931 g/m² provided by Tissa Glasweberei AG and polypropylene (PP) BJ100HP

from Borealis were used. The PP was received in the form of granulates and processed to 0.15 mm thick foils with a Collin extruder to form a model material for investigations. The material properties are summarized in Table 1, with values taken from Werlen et al.,⁴⁷ where an extensive material characterization is presented. Additionally, the values of Henry's constant and the diffusion coefficient for PP were taken from Sato et al.⁵⁴ The areal weight of a matrix ply was measured by weighting polymer foils of known dimensions with a precision scale. The in-plane textile permeability transverse to fiber direction K_{xx} was measured with a custom setup. For the measurements the textile was cut to dimension with a CNC cutter machine, then placed in a cavity with adjustable height which is defined with spacers. Judicious selection of both the number of textile layers and cavity height allows to tailor the fiber volume fraction. During the measurement, a pressurized vessel let silicone oil flow in-plane through the textile which was then collected in a recipient whose weight was continuously measured. Several pressure sensors placed throughout the cavity allowed to measure the pressure and infer the pressure gradient. Finally, the permeability can be measured from the mass flow, density, pressure gradient, cavity height, and width as detailed elsewhere.⁵⁵ Permeability was measured at fiber volume fractions of 0.37 and 0.49 with three repeats and a virgin sample for each new measurement, then the permeability in function of the fiber volume fraction was fitted to the function:

$$K = K_c \cdot \frac{\sqrt{\frac{\nu_f^{max}}{\nu_f} - 1}}{\frac{\nu_f^{max}}{\nu_f} + 1}^3 \quad (29)$$

based on the modified Carman–Kozeny equation proposed by Gutowski et al.^{4,52} Here, K_c is a fitting constant and $\nu_{f,max}$ the maximal hexagonal packing. The variables used for the simulation are listed in Table 1, where A_{tex} and B_{tex} are fitted constants used to describe the quasi-static textile stress response σ_{tex} , which takes the form $A_{tex} \cdot e^{B_{tex} \cdot \nu_f}$ as detailed in Werlen et al.⁴⁷

5 | CASE STUDY

A case study was conducted to numerically validate the model and examine phenomena on geometries that are more complex than a flat plate. Specifically, a flat plate with a stepwise thickness change was selected, whereas four plies of hybrid textile were placed in the thinner part of the plate and twice as many plies in the thicker part. It was considered that the part was pressed in a mold designed to match the thickness of the fully consolidated

TABLE 1 List of the variables that were used in this study and corresponding values.

Variable	Description	Value	Unit
A_{tex}	First fitted constant for textile stress response	0.03	N/m ²
A_{tow}	Tow cross-sectional surface area	1.14×10^{-6}	m ²
A_{tow}^{fj}	First fitted constant for tow fiber volume fraction	8.23×10^{-3}	–
B_{tex}	Second fitted constant for textile stress response	24.2	–
D_{tow}^{fj}	Second fitted constant for tow fiber volume fraction	0.6244	–
D	Diffusion coefficient	5×10^{-9}	m ² /s
F_{app}	Applied force	14.45	kN
G	Diffusion correction factor	2.3×10^{-4}	–
H	Henry's constant	3.6×10^{-5}	mol/Pa·m ³
K_c	Fitted constant for in-plane textile	1.3×10^{-9}	m ²
K_x	In-plane textile permeability	5×10^{-11}	m ²
M_f^A	Areal weight of a textile ply	0.931	kg/m ²
M_m^A	Areal weight of a matrix ply	0.287	kg/m ²
N_1	Number of plies in the thin part of the plate	4	–
N_2	Number of plies in the thick part of the plate	8	–
R_{eq}	Equivalent radius	4.47×10^{-4}	m
R_f	Fiber radius	9	μm
T	Processing temperature	463.15	K
η	Molten polymer viscosity	495	Pa s
$\nu_{f,0}$	Textile fiber volume fraction at rest	0.4378	–
$\nu_{f,max}$	Maximal hexagonal packing	$\frac{\pi}{2\sqrt{3}}$	–
$\nu_{f,tow}$	Tow fiber volume fraction	0.75	–
ρ_m	Density of molten polymer	763	kg/m ³
ρ_f	Density of the textile	2524	kg/m ³

plate in its molten state, which was respectively 3 and 6 mm. In this study, the desired mold geometry was obtained by placing an insert in a custom 170 × 85 mm mold originally meant to produce flat plates, as represented in Figure 5. In the following, the coordinate system defined in Figure 5 is used when describing the position along the plate. Accordingly, the thick part of the plate is located between 0 and 85 mm.

To simulate the consolidation process, the set of equations was implemented in the PDE module of COMSOL Multiphysics[®] 5.4. The problem was reduced to a 2D problem since the consolidation is homogeneous along the plate width. The set of equation was implemented on a 1D domain only, as the change of thickness (second dimension) was implicitly defined in the set of equations. The closing speed in function of time was optimized to satisfy the boundary condition expressed in Equation (24). A mean applied pressure of 1 MPa was selected as the boundary condition, which corresponds to an applied

force of 14.5 kN, and consolidation is simulated for 10 min. The model had 104 elements with mesh refinement close to the thickness change, and was solved with a direct and fully coupled solver with a 0.1 s timestep.

The results indicated that none of the variables were homogeneous, confirming that unit cell models are not sufficient for complex shapes. Figure 6 shows the value distribution of several variables along the plate after a consolidation time of 60 s. The most significant changes in variable values occurred in the middle of the plate where the thickness changes. The thicker part of the plate was subjected to a higher pressure, which led to a more elevated impregnation degree, which resulted in a lower void volume fraction and somewhat higher fiber volume fraction in agreement with Equations (5) and (10).

The evolution of the mean values of the impregnation degree ξ , the fiber volume content ν_f and the porosity ν_g as a function of time is shown in Figure 7. The impregnation

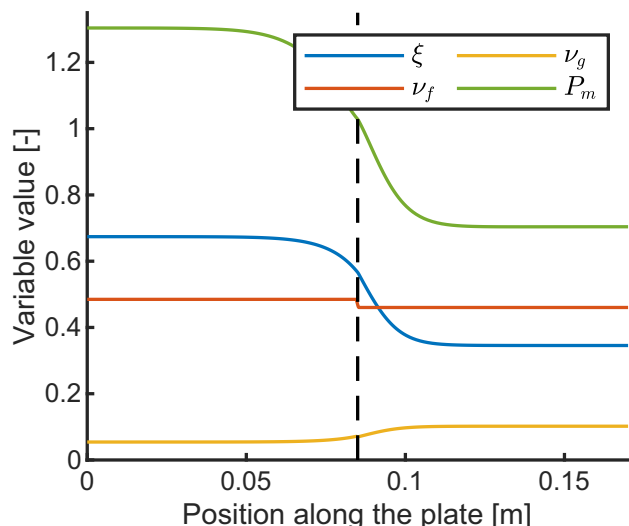


FIGURE 6 Model prediction on the impregnation degree ξ , fiber volume fraction ν_f , void volume fraction ν_g and matrix pressure P_m in function of the position in the mold after 60 s. of consolidation under a mean consolidation pressure of 1 MPa. The dotted line indicates the location of the thickness change.

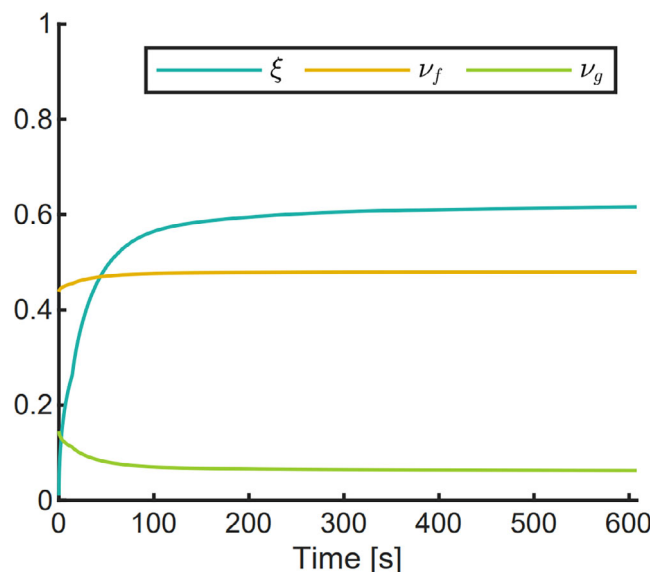


FIGURE 7 Model prediction on the mean impregnation degree ξ , fiber volume fraction ν_f , gas volume fraction ν_g in MPa in function of the consolidation time t .

degree rapidly increased at the beginning of consolidation, after which the curve flattened out. The model also predicted a fast closure speed of 1.1×10^{-4} m/s at the beginning of consolidation, which then sharply decreases to 5.5×10^{-9} m/s after 10 min. This behavior is explained by the dependence of the mold closure speed on the impregnation degree expressed in Equation (23). The mean matrix pressure was equal to the applied pressure defined as the boundary condition due to mechanical equilibrium

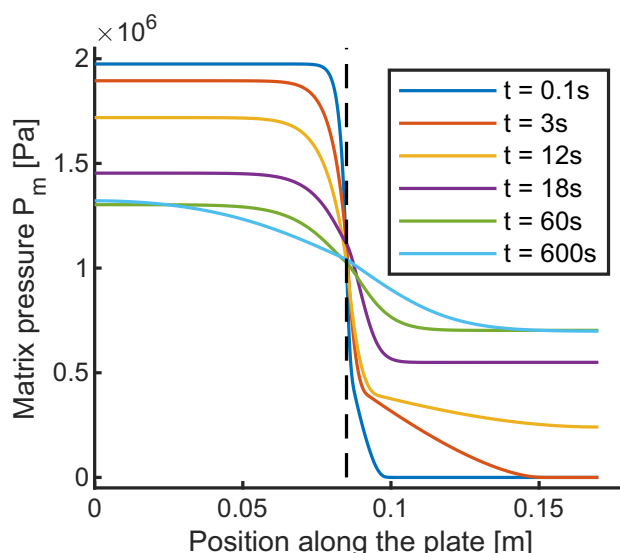


FIGURE 8 Predicted matrix pressure P_m distribution in the mold in function of the consolidation time t . The dotted line indicates the location of the thickness change.

since the textile stress response was predicted to be negligible. All these observations correspond to an expected behavior, very similar to the results described by Werlen et al.⁴⁷ for the 0D case of a homogeneous flat plate.

Figure 8 presents the evolution of the pressure distribution in the plate as a function of time. The composite thickness change is dependent on the impregnation degree and proportional to the number of textile layers, as expressed through Equation (27). Because the change of thickness resulting from impregnation is greater in the thicker part of the step plate, and because the mold fits the fully impregnated plate, at beginning of consolidation only the thicker part of the step plate will be in contact with the mold and under pressure.

A considerable matrix pressure gradient arises in the middle of the plate, as a result of this pressure distribution imbalance. This significant pressure gradient creates an in-plane flow, which can cause fiber disorientation if the tows are dragged along. With progressing impregnation the thickness decreases because voids gets filled as represented in Figure 9. Hence, at some point the thinner part of the plate also comes in contact with the mold and pressure starts to build up there. In Figure 8, this can be observed after 12 s. Overall, the pressure gradient results in an in-plane flow which counteracts the pressure imbalance, as a result the maximal pressure gradient rapidly decreases over time from 4.4×10^8 MPa m^{-1} . at the beginning to 10^7 MPa m^{-1} . after 10 min. Simulation performed with other applied consolidation force—resulting in different mean applied pressure—show that the initial maximum pressure gradient is proportional to the closure speed and applied pressure.

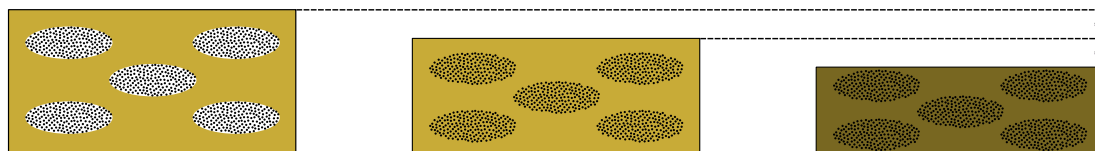


FIGURE 9 Schematic representation of the change of thickness during consolidation. The initial state is shown in the left, the fully impregnated state in the middle and the final state after cooling on the right. The light beige shade indicates molten polymer while the darker shade indicates a solidification. Reproduced with permission from Werlen et al.⁴⁷

6 | EXPERIMENTAL VERIFICATION

Step plates were pressed at different pressures, then possible defects were measured and quantified. As the validation of impregnation was already carried out in Werlen et al.,⁴⁷ the focus of the experimental verification was laid on effects taking place only in complex geometries. The following points, ensuing from the case study, were sought to be demonstrated:

1. In complex geometries in-plane matrix pressure and flow arise and can potentially create defect by altering the textile architecture and disorienting the fibers.
2. During the consolidation of step plates, the highest matrix pressure gradient takes place where the thickness changes, in the middle of the plate. Therefore, this is where the defects should arise.
3. The maximal pressure gradient is proportional to the applied force, therefore higher applied pressures should result in larger defects.

For the experiments, textile plies were cut to the dimensions of the mold with a CNC cutting machine while the thermoplastic foils were cut by hand with a cutter and a stencil. The plies were then placed into the custom plate mold equipped with the insert and temperature sensor, thereby great care was taken not to disturb the textile architecture, which was ensured by visual inspection. The mold containing the plies was placed in a press heated to 200°C with a spacer to avoid applying pressure during heating up, which was then removed when the composite reached processing temperature. This ensured the consolidation process to be identical and comparable to the simulation. The mold was then placed in a cold press and cooled down under the same pressure. Plates were produced with the following pressures, which were kept constant during consolidation: 0.07/0.14/0.5/1/3.5 MPa. The consolidation experiments were performed with two different presses, because a single one could not have covered the whole range of pressures. At low consolidation pressures up to 0.5 MPa, an APV Meyer press was used while at higher pressures experiments were performed with a two-stage Vogt press.

A visual inspection revealed fiber disorientation in some of the produced plates. In the plate consolidated at the lowest pressure, hardly any defect could be observed. However, irregularities were then more pronounced with increasing consolidation pressure. The biggest defects were located in the middle of the plate where the thickness changes, in addition zones where the textile is either stretched or compressed could be observed. This is illustrated in Figure 10, where a close-up of the plates produced at the lowest and highest pressure is shown.

The plates were then analyzed and the defects measured. The deviation from average tow spacing was selected as a method to quantify the defects, because in an ideal plate all the tows of the textile would be perfectly straight and equidistant. To this end, the face of the plate without step was photographed in high resolution with a Nikon D810 camera, together with a scale for reference. The position of the tows were manually measured with the software ImageJ by pin-pointing the left and right edge of each tow along a virtual line parallel to the plate in the x direction. The position of each tow was then inferred as the mean value of the two points, subsequently the distance between two tows d and the average distance between the tows \bar{d} were measured. The deviation from mean spacing Δd is defined in Equation (30):

$$\Delta d = d - \bar{d} \quad (30)$$

The measurements were repeated along three different lines separating the plate in equidistant parts. The defect size Δd was finally measured as the seven-point mean moving average of the defects, to reduce the noise in the single measurement points and identify trends. In all the plates produced, the largest measured defects were located in the middle of the plate where the thickness changes as expected, confirming that the largest pressure gradients arise at this location. Exemplary results for the plates produced with a consolidation pressure of 0.07 and 3.5 MPa are shown in Figure 11A,B. Thereby, the defects were measured along three different lines as mentioned earlier and as represented in Figure 10A.

Measuring the defects of the plate produced at the lowest pressure in Figure 11A confirms that the plate is

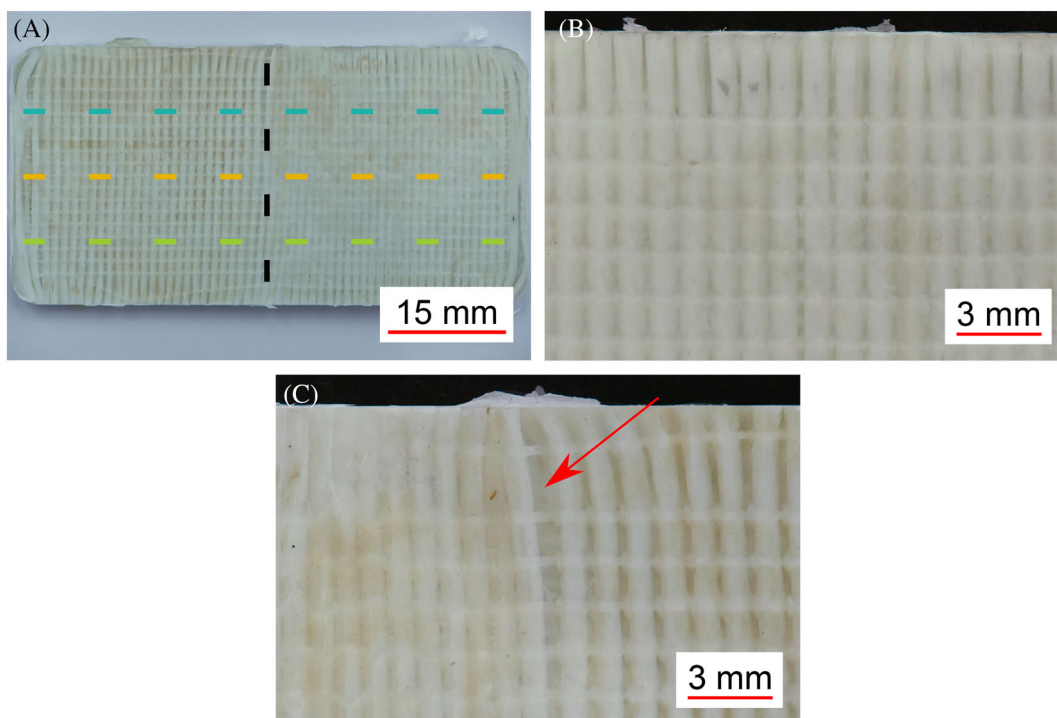


FIGURE 10 Picture of the backside of the plate pressed at 3.5 MPa in (A), whereas the vertical dashed line indicates the location of the step change and the defects were measured along the three horizontal dashed lines. Close up pictures of the backside, in the region of the thickness change, of the plates produced with a consolidation pressure of 0.07 MPa in (B) and 3.5 MPa in (C). The defect is indicated in (C) with a red arrow while almost undisturbed textile geometry can be observed in (B). Additional Pictures can be seen in Appendix F, Figure F1.

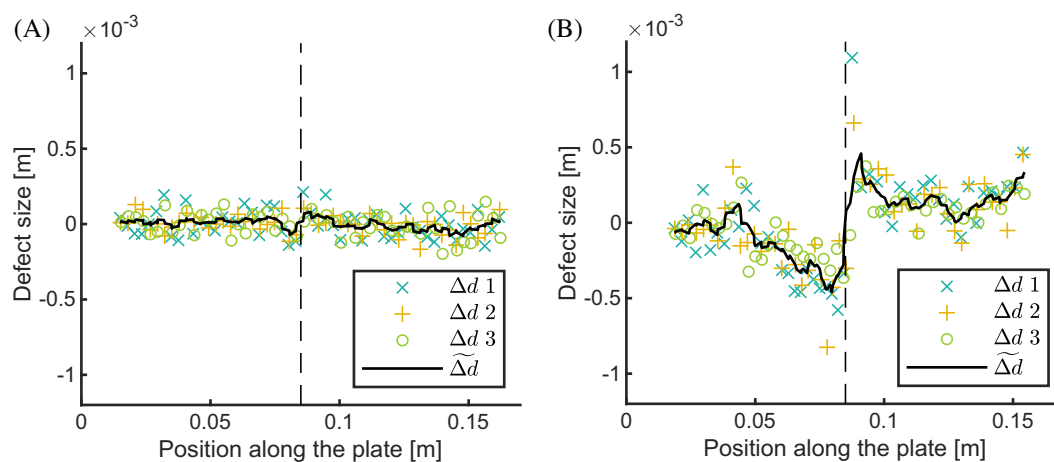


FIGURE 11 Measured defects of the plates pressed at 0.07 MPa in (A) and 3.5 MPa in (B). Δd is the deviation between tow spacing and mean tow spacing, measured along three different lines. $\bar{\Delta d}$ is the moving average of the single measurement points, which is defined in this study as the defect size. The dotted lines indicate the thickness change in the middle of the plate.

nearly defect free and indicates a measurement precision of 1×10^{-4} m, therefore it cannot be excluded that the very small measured defect size are measurement inaccuracies. The single defect points are in the range of $0 \pm 2 \times 10^{-4}$ m, which indicates the measurement accuracy of single points. The defect size along the plate

confirms that applying a moving average helps to reduce noise, as its value remains very close to zero.

Figure 11B is very different and illustrates the presence of fiber displacement. The largest defects are located in the middle of the plate, and the zones where the average defects are positive and negative indicates

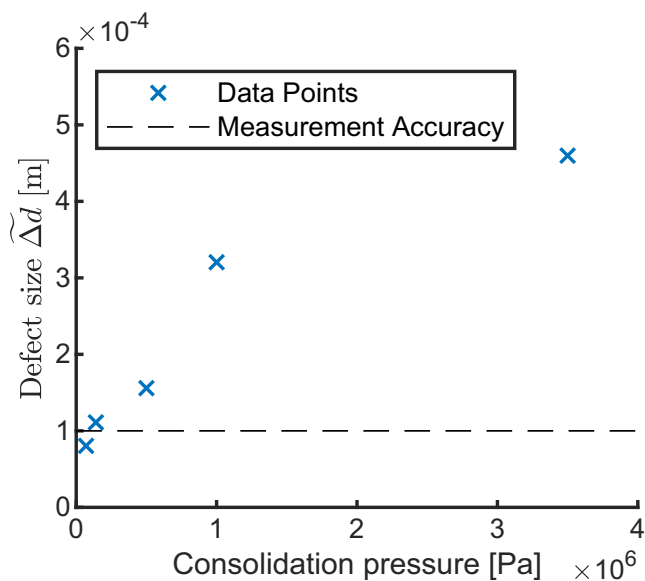


FIGURE 12 Measured maximal defects in step plates produced at different consolidation pressures. The defect size in function of the pressure gradient follow similar trends, since consolidation pressure and pressure gradient are proportional.

respectively stretching and compression, in line with the observations made with the naked eye. The moving average of the defects along single measurement lines are very close to each other, which is expected as all parameters should remain constant along fiber direction.

Figure 12 shows the maximal measured defect size in function of the consolidation pressure. Since larger defects are caused by higher pressure gradient, these observations are therefore in line with the model which predicted maximal matrix pressure gradients proportional to the consolidation pressure. In addition, the largest defects systematically occur as predicted where the plate thickness change, demonstrating the ability of the model to capture the relevant phenomena during consolidation. One can see in Figure 12 that for the virtually defect-free plate pressed at 0.7 bar the defect size is below the detection threshold, while the in plate pressed at 1.4 bar the measured defect is already significant. This indicates a defect formation threshold at a consolidation pressure around 1 bar, which corresponds to a pressure gradient of 45 MPa m⁻¹.

7 | DISCUSSION

The model developed in this study can predict consolidation of free form plates with changing thickness and constant through-thickness properties. The model was implemented in 2D in order to perform experimental verification. Complex phenomena arising in three-dimensional geometries

could be successfully identified and explained. To our best knowledge, fiber disorientation resulting from thickness change during press molding of hybrid textiles has not been documented so far. This work is an intermediate step towards a fully three-dimensional consolidation model, in which the assumption of constant through-thickness properties will be overcome. The 2D implementation in FEM is intended to demonstrate the feasibility and meaningfulness of the approach and for verification purposes. Full FEM implementation of the consolidation model in three-dimension is foreseen as future step, for which it is thought that a dedicated solver is necessary. Since most of the parameters such as impregnation degree are not homogeneous throughout complex parts, the proposed consolidation model can be used in the design phase already to identify critical areas and optimize both design and process.

During consolidation trials on step plates, lower pressures were found to result in smaller defects, however within industrial production this is not a reasonable solution to produce a defect-free part as it also results in significantly larger cycle times. Another solution to minimize defect size would be for example to change the textile orientation. The textile architecture most probably has an influence too, which is however unclear at the moment. It would be useful to develop, in future research, a model predicting the defect size in function of the textile architecture and pressure gradient. Hautefeuille et al.¹⁸ reported a threshold for fiber disorientation for in-plane flow, which depends on the viscosity and flow rate. In this study, consolidating step plates below 1 bar of pressure resulted in defect-free parts and it was found that the threshold of matrix pressure gradient above which fiber disorientation takes place is 45 MPa m⁻¹.

Since pressure gradient is predicted to be maximum at the beginning and then rapidly decrease, another possibility to reduce defect size that should be investigated is to apply first very low pressure and then to gradually increase it. This way of doing could allow to strike a balance between defect minimization and cycle time in order to keep the process relevant for the industry. One last possibility would be to optimize the geometry, for example by smoothing the transition between zones with different thicknesses with ply drop-off.

Since the model can predict a set of properties at each location throughout the part such as porosity and fiber volume fraction, it could be used during the design phase for optimization purposes. In this study, the hybrid textile properties were homogeneous in the plate. Yet, the model can be used on complex shaped with different textiles, textile orientations and areal weights at different locations in the part.

In this study, the model complexity was limited by the assumption that the composite properties are

constant through-thickness. In future work, the model will be fully extended to three dimensions, so that inhomogeneous hybrid textile layups and through-thickness effects can be considered. Through-thickness effects can arise if there is an imbalance of textile stress response for example, as described for example in Studer et al.⁵⁶ or Michaud et al.^{6,7}

In future work, it is planned to validate the model with the high-performance hybrid textile shown in Figure 1 and to measure a set of parameters such as matrix pressure and porosity throughout the part to compare it against model predictions. After fully implementing the model in three dimensions, it should also be validated for more complex geometries and lay-up. It is thought that a dedicated solver is necessary to implement the model fully numerically in three dimensions, in addition further boundary conditions should be implemented. While in this study it was assumed that the mold is rigid, in reality steel is elastic and this should be embedded in the simulation, as this is relevant for high pressure consolidation.

In order to be able to simulate the whole consolidation process, it would be furthermore necessary to implement a thermal simulation in the model and include matrix phase transitions. During a variothermal press cycle and especially for thick parts, the temperature is not homogeneously distributed throughout the part. Since several parameters such as viscosity and solubility of gases in molten polymer have a very strong dependence on temperature, accurately modeling it is of prime importance. Implementing the matrix phase transition such as vitrification and crystallization would allow to properly predict the fiber volume content in solidified state, which differs from the molten state since the matrix density and thus total volume are different as pictured in Figure 6. During cooling down, solidification could also result in pressure gradient and defect formation and this should be investigated in future studies.

The consolidation model proposed in this study allows to determine a variety of parameters in complex shaped composites, and can be used to identifying porosities or zones with potential fiber disorientation during the design phase already. The information about fiber volume fraction and porosity provided by the model could be used as a basis to determine the mechanical properties. Therefore, all the necessary variables to enable optimization of complex-shaped composites are available.

8 | CONCLUSION

In this article, we propose and experimentally verify a three-dimensional consolidation model for hybrid textile.

By adopting a homogenization method, the multi-scale nature of the problem can be bypassed and computational power requirements significantly reduced when compared to a full scale simulation. The model is based on the consolidation model proposed by Werlen et al.,⁴⁷ however the method is applicable to other consolidation models as well. The consolidation model can predict the properties of the part at each location through a set of characteristic parameters such as fiber volume fraction, impregnation degree and porosity.

The model successfully predicted the emergence of matrix pressure gradients in three-dimensional geometries, which can lead to fiber disorientation. Experimental verification confirmed the model predictions, and new mechanisms for the emergence of matrix pressure gradients and defect formation were unveiled and explained. However, model validation with comparison between predicted and measured values, for matrix pressure for instance, remains to be performed in future work.

Current model limitations are the assumptions that the properties are assumed constant through-thickness, however this issue will be addressed in future work. Phase change for the matrix will be introduced, so that consolidation can be predicted in full three-dimensional complexity over the whole production cycle. This will allow to verify model predictions on local characteristic parameters. Finally, the consolidation model presented in this study enables design and process optimization, which shall be investigated in future work.

ACKNOWLEDGMENTS

This work is part of the research project Consolidation of Thermoplastic hybrid yarn materials" ConThP" and is funded by the German Research Foundation [DFG Nr. 394279584] and the Swiss National Science Foundation [200021E/177210/1]. During the preparation of this work, the authors used ChatGPT in order to improve readability and language. The authors kindly thank Mr. Schneeberger and Tissa Glasweberei AG for providing the textiles and for their precious support. Special thanks to Igor Zhylaev for the constructive input regarding model implementation in COMSOL Multiphysics®.

DATA AVAILABILITY STATEMENT

Data sharing is not applicable to this article as no new data were created or analyzed in this study.

ORCID

Vincent Werlen  <https://orcid.org/0000-0002-7802-4139>

Véronique Michaud  <https://orcid.org/0000-0001-5699-740X>

REFERENCES

- Reynolds N, Awang-Ngah S, Williams G, Hughes DJ. Direct processing of structural thermoplastic composites using rapid isothermal stamp forming. *Appl Compos Mater*. 2020;27(1-2):107-115.
- Wysocki M, Toll S, Larsson R. Press forming of commingled yarn based composites: the preform contribution. *Compos Sci Technol*. 2007;67:515-524.
- Wysocki M, Larsson R, Toll S. *Modelling the Consolidation of Partially Impregnated Prepregs*. ICCM17; 2009.
- Gutowski TG, Cai Z, Bauer S, Boucher D, Kingery J, Wineman S. Consolidation experiments for laminate composites. *J Compos Mater*. 1987;21:650-669.
- Bernet N, Michaud V, Bourban PE, Manson J-AE. An impregnation model for the consolidation of thermoplastic composites made from commingled yarns. *J Compos Mater*. 1999;33(8):751-772.
- Michaud V, Manson J-AE. Impregnation of compressible fiber mats with a thermoplastic resin. Part I: theory. *J Compos Mater*. 2001;35(13):1150-1173.
- Michaud V, Törnqvist R, Manson J-AE. Impregnation of compressible fiber mats with a thermoplastic resin. Part II: experiments. *J Compos Mater*. 2001;35(13):1174-1200.
- Danzi M, Schneeberger C, Ermanni P. A model for the time-dependent compaction response of woven fiber textiles. *Compos Part A: Appl Sci Manuf*. 2018;105:180-188.
- Werlen V, Rytka C, Michaud V. A numerical approach to characterize the viscoelastic behaviour of fibre beds and to evaluate the influence of strain deviations on viscoelastic parameter extraction. *Compos Part A: Appl Sci Manuf*. 2021;143(October 2020):106315.
- Epstein PS, Plesset MS. On the stability of gas bubbles in liquid-gas solutions. *J Chem Phys*. 1950;18(11):1505-1509.
- Lundström TS. Measurement of void collapse during resin transfer moulding. *Compos Part A: Appl Sci Manuf*. 1997;28(3):201-214.
- Schuler S, Advani SG. Transverse squeeze flow of concentrated aligned fibers in viscous fluids. *J Non-Newtonian Fluid Mech*. 1996;65:47-74.
- Chun HJ, Shin JY, Daniel IM. Effects of material and geometric nonlinearities on the tensile and compressive behavior of composite materials with fiber waviness. *Compos Sci Technol*. 2001;61(1):125-134.
- Ghnatios C, Abisset-Chavanne E, Binetruy C, Chinesta F, Advani SG. 3D modeling of squeeze flow of multiaxial laminates. *J NonNewtonian Fluid Mech*. 2016;234:188-200.
- Picher-Martel GP, Levy A, Hubert P. Compression moulding of carbon/PEEK randomly-oriented strands composites: a 2D finite element model to predict the squeeze flow behaviour. *Compos Part A: Appl Sci Manuf*. 2016;81:69-77.
- Sorba G, Binetruy C, Leygue A, Comas-Cardona S. Squeeze flow in heterogeneous unidirectional discontinuous viscous prepreg laminates: experimental measurement and 3D modeling. *Compos Part A: Appl Sci Manuf*. 2017;103:196-207.
- Servais C, Luciani A, Manson J-AE. Squeeze flow of concentrated long fibre suspensions: experiments and model. *J Non-Newtonian Fluid Mech*. 2002;104:165-184.
- Hautefeuille A, Comas-Cardona S, Binetruy C. Mechanical signature and full-field measurement of flow-induced large in-plane deformation of fibrous reinforcements in composite processing. *Compos Part A: Appl Sci Manuf*. 2019;118(May 2018):213-222.
- Hautefeuille A, Comas-Cardona S, Binetruy C. Consolidation and compression of deformable impregnated fibrous reinforcements: experimental study and modeling of flow-induced deformations. *Compos Part A: Appl Sci Manuf*. 2020;131:105768.
- Wood JR, Bader MG. Void control for polymer-matrix composites (1): theoretical and experimental methods for determining the growth and collapse of gas bubbles. *Compos Manuf*. 1994;5(3):139-147.
- Vaxman A, Narkis M, Siegmann A, Kenig S. Void formation in shortfiber thermoplastic composites. *Polym Compos*. 1989;10(6):449-453.
- Saenz-castillo D, Mart'in MI, Calvo S, Rodriguez-lence F, Güemes A. Effect of processing parameters and void content on mechanical properties and NDI of thermoplastic composites. *Compos Part A: Appl Sci Manuf*. 2019;121(March):308-320.
- Zhang D, Heider D, Gillespie JW. Void reduction of high-performance thermoplastic composites via oven vacuum bag processing. *J Compos Mater*. 2017;51(30):4219-4230.
- Zhang D. *Void Consolidation of Thermoplastic Composites Via NonAutoclave Processing*, Dissertation, University of Delaware. 2017.
- Niaki SA, Forghani A, Vaziri R, Poursartip A. A two-phase integrated flow-stress process model for composites with application to highly compressible phases. *Mech Mater*. 2017;109:51-66.
- Niaki SA, Forghani A, Vaziri R, Poursartip A. A three-phase integrated flow-stress model for processing of composites. *Mech Mater*. 2018;117(March 2017):152-164.
- Khoei AR, Mohammadnejad T. Numerical modeling of multiphase fluid flow in deforming porous media: a comparison between two- and threephase models for seismic analysis of earth and rockfill dams. *Comput Geotech*. 2011;38(2):142-166.
- Nagel F, Meschke G. An elasto-plastic three phase model for partially saturated soil for the finite element simulation of compressed air support in tunnelling. *Int J Numer Anal Methods Geomech*. 2009;34:605-625.
- Kuentzer N, Simacek P, Advani SG, Walsh S. Correlation of void distribution to VARTM manufacturing techniques. *Compos Part A: Appl Sci Manuf*. 2007;38(3):802-813.
- Tan H, Pillai KM. Multiscale modeling of unsaturated flow in dual-scale fiber preforms of liquid composite molding I: isothermal flows. *Compos Part A: Appl Sci Manuf*. 2012;43(1):1-13.
- Wysocki M, Larsson R, Toll S. Hydrostatic consolidation of commingled fibre composites. *Compos Sci Technol*. 2005;65(10):1507-1519.
- Rouhi MS, Wysocki M, Larsson R. Modeling of coupled dual-scale flowdeformation processes in composites manufacturing. *Compos Part A: Appl Sci Manuf*. 2013;46:108-116.
- Rouhi MS. *Poromechanical Modeling of Composites Manufacturing*, Doctoral thesis, Chalmers University of Technology. 2015.
- Rouhi MS, Wysocki M, Larsson R. Simulation of 3D Rtm process using solid Shell element. *14th International Conference on Flow Processes in Composite Materials*. Vol 3; 2018.
- Phillips R, Akyüz DA, Manson J-AE. Prediction of the consolidation of woven fibre-reinforced thermoplastic composites. Part I. Isothermal case. *Compos Part A: Appl Sci Manuf*. 1998;29:395-402.
- Rozant O, Michaud V, Bourban PE, Manson J-AE. A model for the consolidation of warp-knitted reinforced laminates. *Polym Compos*. 2001;22(3):432-443.

37. Klinkmüller V, Um MK, Steffens M, Friedrich K, Kim BS. A new model for impregnation mechanisms in different GF/PP commingled yarns. *Appl Compos Mater*. 1995;1:351-371.
38. Groupe WJ, Akkerman R. Consolidation process model for film stacking glass/PPS laminates. *Plast Rubber Compos*. 2010;39(3-5):208-215.
39. Kobayashi S, Tsukada T, Morimoto T. Resin impregnation behavior in carbon fiber reinforced polyamide 6 composite: effects of yarn thickness, fabric lamination and sizing agent. *Compos Part A: Appl Sci Manuf*. 2017;101:283-289.
40. Van West BP, Pipes RB, Advani SG. The consolidation of commingled thermoplastic fabrics. *Polym Compos*. 1991;12:417-427.
41. Jespersen ST, Wakeman MD, Michaud V, Cramer D, Manson J-AE. Film stacking impregnation model for a novel net shape thermoplastic composite preforming process. *Compos Sci Technol*. 2008;68:1822-1830.
42. Michaud V, Mortensen A. Infiltration processing of fibre reinforced composites: governing phenomena. *Compos Part A: Appl Sci Manuf*. 2001;32:981-996.
43. Michaud V, Sommer JL, Mortensen A. Infiltration of fibrous preforms by a pure metal: Part V. Influence of preform compressibility. *Metall Mater Trans A: Phys Metall Mater Sci*. 1999;30(2):471-482.
44. Sommer JL, Mortensen A. Forced unidirectional infiltration of deformable porous media. *J Fluid Mech*. 1996;311:193-217.
45. Hou M, Ye L, Lee HJ, Mai YW. Manufacture of a carbon-fabricreinforced polyetherimide (CF/PEI) composite material. *Compos Sci Technol*. 1998;58(2):181-190.
46. Dong C. Effects of process-induced voids on the properties of fibre reinforced composites. *J Mater Sci Technol*. 2016;32(7):597-604.
47. Werlen V, Vocke R, Brauner C, Dransfeld C, Michaud V, Rytka C. A model for the consolidation of hybrid textiles considering air entrapment, dissolution and diffusion. *Compos Part A: Appl Sci Manuf*. 2023;166(December 2022):107413.
48. Pickett AK, Creech G, Luca PD. Simplified and advanced simulation methods for prediction of fabric draping methods for prediction of fabric draping. *Revue Europ'eenne Des El'ements Finis*. 2005;14:677-691.
49. Chen B, Govindaraj M. A physically based model of fabric drape using flexible Shell theory. *Text Res J*. 1995;65(6):324-330.
50. Breen DE, House DH, Wozny MJ. A particle-based model for simulating the draping behavior of woven cloth. *Text Res J*. 1994;64(11):663-685.
51. Darcy H. Les fontaines publiques de la ville de Dijon, Dalmont, Paris. 1856.
52. Carman PC. Fluid flow through granular beds. *Process Safety Environ Protect Trans Inst Chem Eng Part B*. 1997;75:32-48.
53. Gebart B. Permeability of unidirectional reinforcements for RTM. *J Compos Mater*. 1992;26(8):1100-1133.
54. Sato Y, Fujiwara K, Takikawa T, Sumarno S, Takishima HM. Solubilities and diffusion coefficients of carbon dioxide and nitrogen in polypropylene, high-density polyethylene, and polystyrene under high pressures and temperatures. *Fluid Phase Equilib*. 1999;162(1-2):261-276.
55. Arbter R, Beraud JM, Binetruy C, et al. Experimental determination of the permeability of textiles: a benchmark exercise. *Compos Part A: Appl Sci Manuf*. 2011;42:1157-1168.
56. Studer J, Dransfeld C, Cano JC, et al. Effect of fabric architecture, compaction and permeability on through thickness

thermoplastic melt impregnation. *Compos Part A: Appl Sci Manuf*. 2019;122:45-53.

How to cite this article: Werlen V, Rytka C, Dransfeld C, Brauner C, Michaud V. A multiscale consolidation model for press molding of hybrid textiles into complex geometries. *Polym Compos*. 2024;1-19. doi:10.1002/pc.28139

APPENDIX A: DERIVATION OF FIBER VOLUME FRACTIONS

The fiber and gas volume fraction temporal change reads, based on Equations (1) and (6):

$$\frac{\partial \nu_f}{\partial t} = \frac{\partial V_f}{\partial t} \frac{1}{V} = -V_f \frac{1}{V^2} \frac{\partial V}{\partial t} \quad (\text{A1})$$

$$\frac{\partial \nu_g}{\partial t} = \frac{\partial V_g}{\partial t} \frac{1}{V} = \frac{1}{V} \frac{\partial V_g}{\partial t} - V_g \frac{1}{V^2} \frac{\partial V}{\partial t} \quad (\text{A2})$$

The temporal volume change reads, using Equations (3) and (6):

$$\frac{\partial V}{\partial t} = \frac{\partial V_f}{\partial t} + \frac{\partial V_m}{\partial t} + \frac{\partial V_g}{\partial t} = \frac{\partial V_m}{\partial t} + \frac{\partial V_g}{\partial t} \quad (\text{A3})$$

The variation of the gas volume over time can be described on the basis of Equation (5) by inserting Equations (1), (4), and (6), and neglecting changes in tow fiber volume fraction $\nu_{f,tow}$ since the tow is assumed incompressible:

$$\begin{aligned} \frac{\partial V_g}{\partial t} &= \frac{\partial}{\partial t} (V_{tow} - V_{tow,impr.}) (1 - \nu_{f,tow}) \\ &= \frac{\partial}{\partial t} (V_{tow} - \xi V_{tow}) (1 - \nu_{f,tow}) \\ &= \frac{\partial}{\partial t} \left((1 - \xi) \frac{V_f}{\nu_{f,tow}} \right) (1 - \nu_{f,tow}) \\ &= V_f \frac{1 - \nu_{f,tow}}{\nu_{f,tow}} \frac{\partial}{\partial t} (1 - \xi) \\ &= -V_f \frac{1 - \nu_{f,tow}}{\nu_{f,tow}} \frac{\partial \xi}{\partial t} \end{aligned} \quad (\text{A4})$$

Inserting this result into the previous equation yields:

$$\frac{\partial V}{\partial t} = \frac{\partial V_m}{\partial t} - V_f \frac{1 - \nu_{f,tow}}{\nu_{f,tow}} \frac{\partial \xi}{\partial t} \quad (\text{A5})$$

Inserting it back into Equation (A1) together with Equation (1) yields:

$$\begin{aligned} \frac{\partial \nu_f}{\partial t} &= -V_f \frac{1}{V^2} \frac{\partial V}{\partial t} \\ &= -\frac{\nu_f}{V} \frac{\partial V_m}{\partial t} + \nu_f^2 \frac{1 - \nu_{f,tow}}{\nu_{f,tow}} \frac{\partial \xi}{\partial t} \end{aligned} \quad (A6)$$

For the gas volume fraction inserting Equations (A5), (A4), and (1) into Equation (A2) yields:

$$\begin{aligned} \frac{\partial \nu_g}{\partial t} &= \frac{1}{V} \frac{\partial V_g}{\partial t} - \frac{\nu_g}{V} \left[\frac{\partial V_m}{\partial t} + \frac{\partial V_g}{\partial t} \right] \\ &= (\nu_g - 1) \left(\nu_f \frac{1 - \nu_{f,tow}}{\nu_{f,tow}} \frac{\partial \xi}{\partial t} \right) - \frac{\nu_g}{V} \frac{\partial V_m}{\partial t} \end{aligned} \quad (A7)$$

APPENDIX B: MATRIX VOLUME CHANGE

We consider the infinitesimal trapezoid as shown in Figure B1 with dimensions Δx , Δy in the x and y directions, height $h(x,y)$ linearly depending on x and y in the z direction and volume V . In the following, the height of the corners are referred to as h_1 , h_2 , h_3 , and h_4 , the mid side heights in function of either x or y as $h_{12}(x)$, $h_{13}(y)$, $h_{34}(x)$, and $h_{24}(y)$, their average value \bar{h}_{ij} and the average height of the trapezoid h .

To resolve the temporal change of matrix volume Darcy's law⁵¹ is applied to the four sides of the trapezoid, no matrix flowing through either the top or bottom surface since the through-thickness parameters, including matrix pressure, are assumed constant:

$$\frac{1}{V} \frac{\partial V_m}{\partial t} = \frac{1}{V} \left[\begin{aligned} &\int_y^{y+\Delta y} \int_z^{z+h_{13}(y)} -\frac{K_x}{\eta} \frac{\partial P_m}{\partial x} dz dy \\ &-\int_y^{y+\Delta y} \int_z^{z+h_{24}(y)} -\frac{K_x}{\eta} \frac{\partial P_m}{\partial x} dz dy \\ &+\int_x^{x+\Delta x} \int_z^{z+h_{34}(x)} -\frac{K_y}{\eta} \frac{\partial P_m}{\partial y} dz dx \\ &-\int_x^{x+\Delta x} \int_z^{z+h_{12}(x)} -\frac{K_y}{\eta} \frac{\partial P_m}{\partial y} dz dx \end{aligned} \right] \quad (B1)$$

For the continuum formulation we let Δx and Δy tend to zero, which implies that $K_x, K_y, \eta, \frac{\partial P}{\partial x}$ and $\frac{\partial P}{\partial y}$ can be considered constant in the volume and taken out of the integral. This leaves only a surface integral which is straightforward to solve, therefore the previous equation becomes:

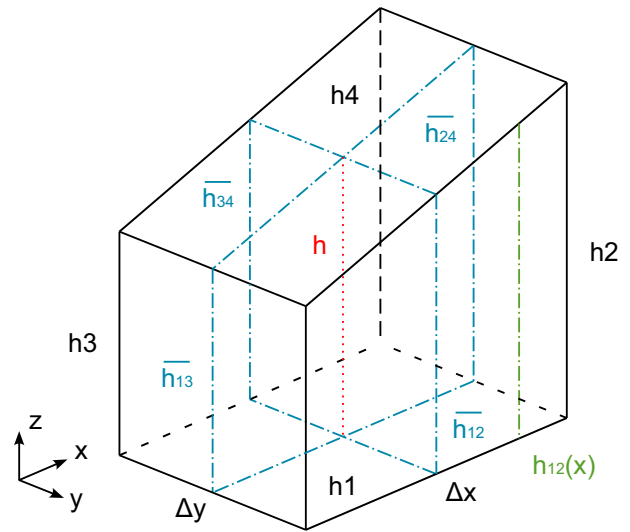


FIGURE B1 Representation of the trapezoid unit cell.

$$\frac{1}{V} \frac{\partial V_m}{\partial t} = \frac{1}{V} \left[\begin{aligned} &\frac{K_x \Delta \bar{h}_{24} \Delta y}{\eta} \frac{\partial P_m(x + \Delta x)}{\partial x} \\ &-\frac{K_x \bar{h}_{13} \Delta y}{\eta} \frac{\partial P_m(x)}{\partial x} \\ &+\frac{K_y \bar{h}_{12} \Delta y}{\eta} \frac{\partial P_m(y + \Delta y)}{\partial y} \\ &-\frac{K_y \bar{h}_{34} \Delta y}{\eta} \frac{\partial P_m(y)}{\partial y} \end{aligned} \right] \quad (B2)$$

Simple geometry considerations allow to write V as:

$$V = \Delta x \cdot \Delta y \cdot h \quad (B3)$$

In addition, the change of average height in x and y directions $\Delta \bar{h}_x$ and $\Delta \bar{h}_y$ are expressed through Equation (B4) and inserting it back yields Equation (B5):

$$\begin{aligned} h_{24} &= h_{13} + \Delta h_x \quad h_{12} = h_{34} + \Delta h_y \\ \frac{1}{V} \frac{\partial V_m}{\partial t} &= \left[\frac{K_x \bar{h}_{13}}{xh} \left(\frac{\partial P_m(x + \Delta x)}{\partial x} - \frac{\partial P_m(x)}{\partial x} \right) \right] \end{aligned} \quad (B4)$$

$$\begin{aligned} &\eta \Delta \\ &+\frac{K_x \Delta \bar{h}_x}{\eta \Delta x h} \frac{\partial P_m(x + \Delta x)}{\partial x} \\ &+\frac{K_y \bar{h}_{34}}{\eta \Delta y h} \left(\frac{\partial P_m(y + \Delta y)}{\partial y} - \frac{\partial P_m(y)}{\partial y} \right) \\ &+\frac{K_y \Delta \bar{h}_y}{\eta \Delta y \cdot h} \frac{\partial P_m(y + \Delta y)}{\partial y} \end{aligned} \quad (B5)$$

As Δx and Δy tend to zero \bar{h}_{13} and \bar{h}_{34} tend towards h and we can express the equations, based on the definition of a derivative, as:

$$\begin{aligned} \frac{1}{V} \frac{\partial V_m}{\partial t} &= \left[\frac{K_x}{\eta} \frac{\partial^2 P_m}{\partial x^2} + \frac{K_x}{\eta \bar{h}} \frac{\partial h}{\partial x} \frac{\partial P_m}{\partial x} + \frac{K_y}{\eta} \frac{\partial^2 P_m}{\partial y^2} + \frac{K_y}{\eta \bar{h}} \frac{\partial h}{\partial y} \frac{\partial P_m}{\partial y} \right] \\ &= \frac{\vec{\nabla} K \vec{\nabla} P_m}{\eta} + \frac{\vec{\nabla} h^T K \vec{\nabla} P_m}{h \eta} \end{aligned} \quad (\text{B6})$$

APPENDIX C: DERIVATIVE OF IMPREGNATION DEGREE

In Equation (C1), the derivative of ξ is expressed by inserting Equation (13) and developing the expression considering that R_{eq} is constant. Then, Equation (14) is inserted to replace the term $r \frac{\partial r}{\partial t}$ and finally $\frac{r}{R_{eq}}$ is expressed in terms of impregnation degree using Equation (13).

$$\begin{aligned} \frac{\partial \xi}{\partial t} &= \frac{\partial R_{eq}^2 - r^2}{\partial t R_{eq}^2} \\ &= \frac{-2}{R_{eq}^2} r \frac{\partial r}{\partial t} \\ &= \frac{-2 K_\mu (P_m + P_c - P_g)}{R_{eq}^2 \eta (1 - \nu_{f,tow})} \frac{1}{\ln \left(\frac{r}{R_{eq}} \right)} \\ &= \frac{-2 K_\mu (P_m + P_c - P_g)}{R_{eq}^2 \eta (1 - \nu_{f,tow}) \ln(\sqrt{\xi} - 1)} \end{aligned} \quad (\text{C1})$$

APPENDIX D: DERIVATIVE OF THICKNESS

The temporal change of height reads, combining Equations (22), (A.5), and based on the volume definition of the trapezoidal unit cell, as:

$$\begin{aligned} \frac{\partial h}{\partial t} &= \frac{1}{\Delta x \cdot \Delta y} \frac{\partial V}{\partial t} = \frac{h}{V} \frac{\partial V}{\partial t} \\ &= \frac{h}{V} \left[\frac{\partial V_m}{\partial t} - V_f \frac{1 - \nu_{f,tow}}{\nu_{f,tow}} \frac{\partial \xi}{\partial t} \right] \end{aligned} \quad (\text{D1})$$

inserting Equations (21), (1), and (B6) yields:

$$\begin{aligned} \frac{v}{h} &= \frac{1}{V} \left[\frac{\partial V_m}{\partial t} - V_f \frac{1 - \nu_{f,tow}}{\nu_{f,tow}} \frac{\partial \xi}{\partial t} \right] \\ &= \frac{\vec{\nabla} K \vec{\nabla} P_m}{\eta} + \frac{(\vec{\nabla} h)^T K \vec{\nabla} P_m}{h \cdot \eta} - \nu_f \frac{1 - \nu_{f,tow}}{\nu_{f,tow}} \frac{\partial \xi}{\partial t} \end{aligned} \quad (\text{D2})$$

APPENDIX E: INITIAL CONDITIONS

To describe the height of the composite, Equation (22) is first combined with Equation (3), then Equations (2) and (5) are inserted. The final equation is obtained by inserting the areal weight M_m^A and M_f^A of the fibers and matrix in a ply and the local number of plies N :

$$\begin{aligned} h &= \frac{V}{\Delta x \cdot \Delta y} = \frac{V_m}{\Delta x \cdot \Delta y} + \frac{V_f}{\Delta x \cdot \Delta y} + \frac{V_g}{\Delta x \cdot \Delta y} \\ &= \frac{M_m}{\Delta x \cdot \Delta y \cdot \rho_m} + \frac{M_f}{\Delta x \cdot \Delta y \cdot \rho_f} \\ &\quad + \frac{M_f}{\Delta x \cdot \Delta y \cdot \rho_f} (1 - \xi) \frac{1 - \nu_{f,tow}}{\nu_{f,tow}} \\ &= \frac{N \cdot M_m^A}{\rho_m} + \frac{N \cdot M_f^A}{\rho_f} \left(1 + (1 - \xi) \cdot \frac{1 - \nu_{f,tow}}{\nu_{f,tow}} \right) \end{aligned} \quad (\text{E1})$$

The volume fractions of the matrix, fiber and gas are obtained on the basis of Equation (1), the phase volumes are then expressed in function of areal weight in a similar fashion to Equation (E1):

$$\begin{aligned} \nu_f &= \frac{V_f}{V} = \frac{M_f}{\rho_f \cdot h \cdot \Delta x \cdot \Delta y} = \frac{N \cdot M_f^A}{\rho_m \cdot h} \\ \nu_m &= \frac{V_m}{V} = \frac{M_m}{\rho_m \cdot h \cdot \Delta x \cdot \Delta y} = \frac{N \cdot M_m^A}{\rho_m \cdot h} \\ \nu_g &= \frac{V_g}{V} = \frac{N \cdot M_f^A}{\rho_f \cdot h} \cdot (1 - \xi) \cdot \frac{1 - \nu_{f,tow}}{\nu_{f,tow}} \end{aligned} \quad (\text{E2})$$

APPENDIX F: ADDITIONAL PICTURES

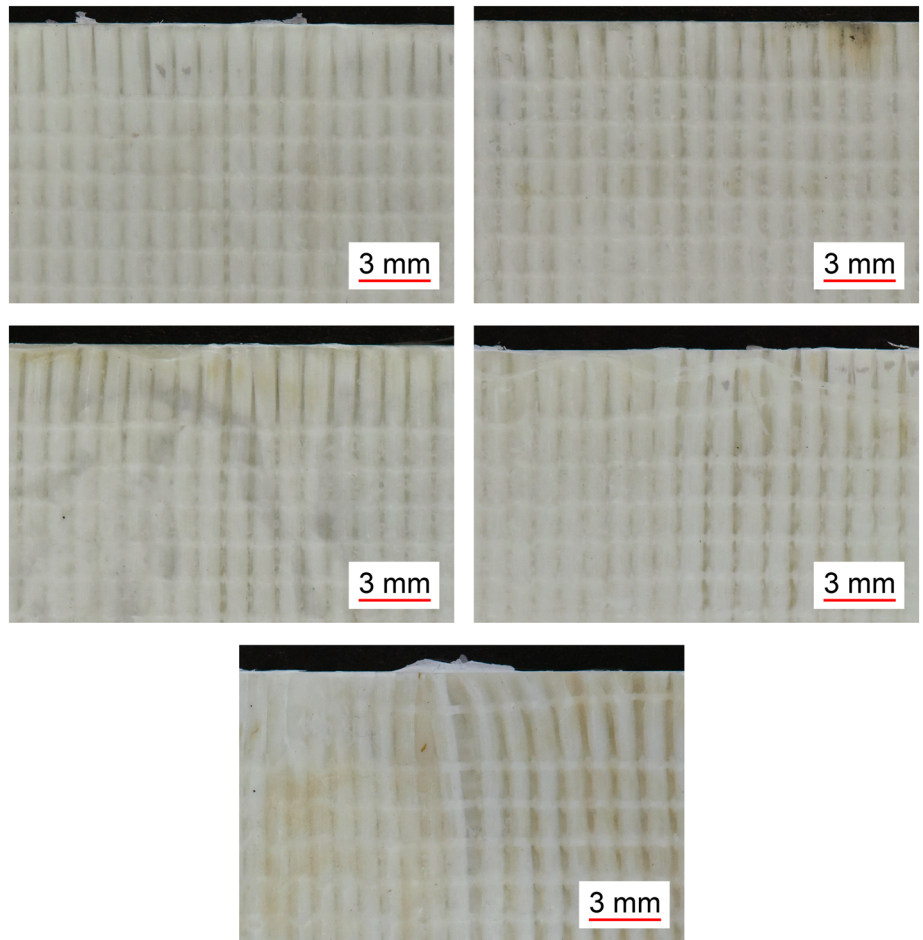


FIGURE F1 Close up pictures of the backside, in the region of the thickness change, of the plates pressed at 0.07, 0.14, 0.5, 1, and 3.5 MPa in (A–F).